Geochemical Characterization and Petrogenesis of the Burji Younger Granite Complex, North-Central Nigeria: Implications for Rare-Metal Mineralization

T. C. Gbaa[1*], A. I. Haruna[1], A. I. Jibrin[1], U. S. Umar[1], M. A. Hassan[1], M. Wada[1], H. Y. Mohammed[1]
*Corresponding author: T. C. Gbaa;
Email: terngugbaa@gmail.com
[1] Department of Geology, Abubakar
Tafawa Balewa University, Bauchi, Nigeria.

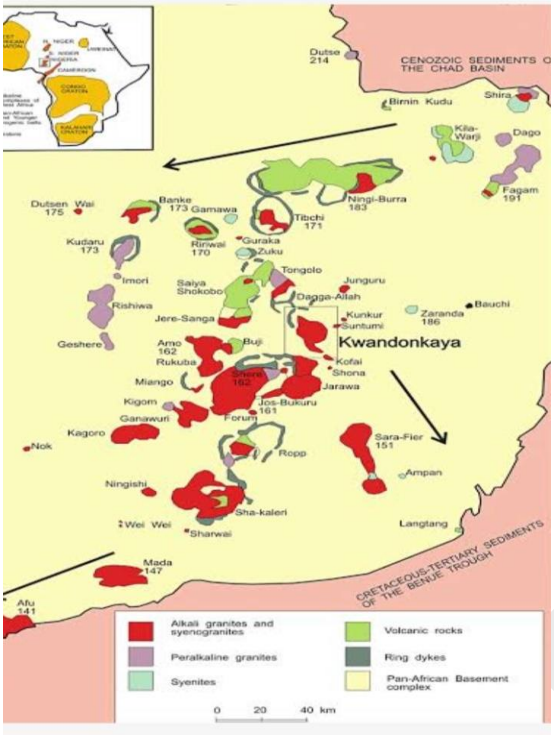
https://doi.org/10.56201/ijaes.vol.12.no11.2026.pg94.107

Abstract
The Burji Younger Granite complex located in Central Nigeria forms part of the Mesozoic Nigerian Younger Granite Province, characterized by anorogenic magmatism and a range of granite, syenite and volcanic lithologies. This study examines the geochemical characteristics and petrogenesis of rocks exposed on the north-western flank of the complex, with focus on the implications for rare-metal mineralization. The investigation integrates geological field mapping, petrographic examination, energy-dispersive X-ray fluorescence (ED-XRF) whole-rock analyses and atomic absorption spectrometry (AAS) lithium determinations. Eighteen representative rock samples were collected; thirteen were selected for thin-section and fifteen for whole-rock geochemical analysis, while three samples were analysed for lithium by AAS. The mapped and petrographically characterized rock units consist of alkali-feldspar granite, syenite, quartz monzonite, rhyolite, trachydacite and pegmatite. The principal felsic samples contain 66.1–75.1 wt.% SiO_2, although two reported analyses (TB L14B and TB L11B) are compositionally anomalous and require verification. The dataset records elevated and variable Rb (9.92–1750 ppm), Nb (15.8–905 ppm), Zr (115–3960 ppm) and Y (33.3–847 ppm), together with reported LREE concentrations reaching 437 ppm La, 396 ppm Ce and 375 ppm Nd. Pearce-type discrimination plots place the granitoids predominantly in the within-plate granite field. Elevated alkali concentrations coupled with undetected MgO and pronounced CaO depletion in several samples, accompanied by negative Sr anomalies, demonstrates an evolved A type geochemical signature indicative of significant feldspar fractionation. AAS results demonstrates 7,229–15,320 ppm Li (0.7229–1.532 wt.% Li), equivalent to approximately 1.56–3.30 wt.% Li_2O in the three selected samples. These lithium results are pronounced reconnaissance indicators but do not confirm mineral hosts, grade continuity or an economic resource. Overall, the results identify the Burji complex as a geochemically prospective evolved granite system for follow-up investigation of Li, Nb–Ta, Zr, Y and REE mineralization.

Keywords: *Burji Ring Complex; Younger Granites; A-type granite; geochemistry; petrogenesis; lithium; rare earth elements; high-field-strength elements; Nigeria.*

1. Introduction

The Nigerian Younger Granite Province constitutes part of an extensive north –south trending belt of alkaline anorogenic magmatism extending from the Hoggar – Air region of Niger republic towards the margins of the Benue trough represented by the Afu ring complex as the southernmost Nigerian occurrence. The province is characterized by circular to elliptical ring complexes, with more than 50 recognized complexes (MacLeod et al 1971; Kinnaird, 1985). Regional studies have confirmed that these complexes form part of a broader magmatic trend extending for approximately 1,250 km along the ninth meridian, with a general southward decrease in emplacement age from the older northern centres to the Mesozoic Nigerian complexes (Bowden et al 1976). The province contains numerous ring complexes composed of granitic and syenitic plutons, volcanic rocks and associated dykes. Their emplacement is commonly related to intracontinental extension and anorogenic magmatism, characterized by high level alkaline plutonic and volcanic activity, and the development of ring-fracture systems. Younger Granite complexes are known for their petrological diversity and economic importance because evolved magmatic systems and their late-magmatic fluids may concentrate tin, niobium, tantalum, tungsten, zirconium and rare earth elements (REE), in addition to other critical metals (Eby, 1992; Whalen et al., 1987; Pirajno, 2014; Vonopartis et al., 2021). It has generated significant interest as an important metallogenic domain for understanding the relationship between alkaline magmatism, magmatic differentiation and hydrothermal mineralization (Bowden & Kinnaird 1984). The Burji Ring Complex is one of the less comprehensively documented members of the province with a plutonic-dominated north-western sector and a volcanic component within the broader complex. The study area is located within Lere Sheet 147, approximately 30 km north of Jos, around 10°07′–10°13′N and 8°50′–8°55′E with an estimated area of 20–25 km². This study integrated the regional geological context, field mapping and structural measurements, petrography, whole-rock geochemistry and the assessment of lithium and REE potential. The field component records alkali-feldspar granite, syenite, quartz monzonite, rhyolite, trachydacite and pegmatite, together with quartz veins, joints, fractures and dyke-like bodies. Petrographic observations identify quartz, alkali feldspar, plagioclase/albite, biotite, muscovite and opaque accessory phases. Perthitic and exsolution textures, interlocking crystals and porphyritic volcanic textures are consistent with crystallization across intrusive and shallow volcanic environments. Structural analysis identifies a dominant N–S trend and subsidiary NE–SW and NW–SE trend which is consistent with the N-S alignment of these anorogenic complexes and the associated structural trends of the basement complex, signifying basement control in these emplacement.(Bowden 1976, Rahaman et al 1984, Kinnaird 1985, Aga T & Haruna A.I 2020) The identified ring-related faults, block displacement and rhyolitic bodies are interpreted in terms of cauldron faulting and subsidence. These structures are relevant to the petrogenetic interpretation because ring faults, fractures and veins can provide pathways for late-magmatic and hydrothermal fluids. Pegmatitic material is reported along ridge flanks and topaz is associated in the field with rhyolitic settings. These observations are treated here as field relationships rather than proof of a specific ore assemblage.



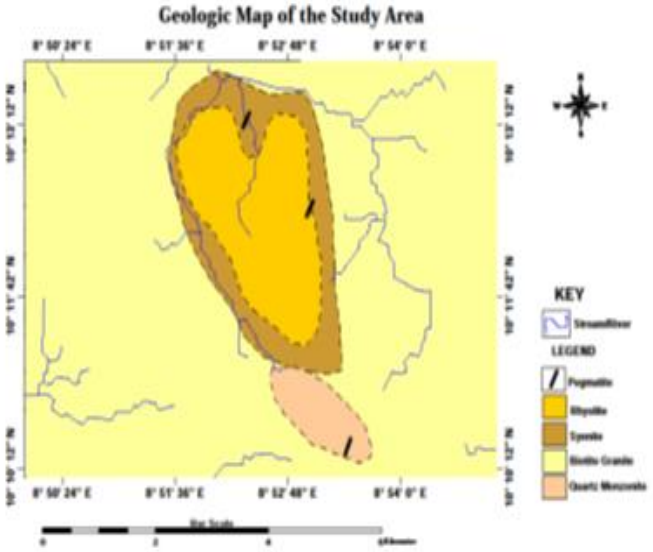


Figure 1 Distribution of Younger Granite complexes and principal lithological groupings Source Emmanuel Sakoma and Robert F martin (Source Canadian Mineralogist 2011). Figure 2 Geological map of the area

The Burji complex is situated within the central part of the Nigerian Younger Granite Province. The regional distribution map illustrates the spatial association of ring complexes and the principal lithological groupings, including alkali granites and syenogranites, peralkaline granites, syenites, volcanic rocks and ring dykes. The Burji ring complex is shown among the complexes north of the Jos–Bukuru cluster. This regional framework places the study within a province in which repeated intrusive and volcanic activity was localized along major crustal structures (Figure 1). The geological map illustrates the distribution and delineation of the lithological units comprising of alkali feldspar granite, syenite, quartz monzonite, rhyolite, trachydacite, pegmatite units, and their contacts. At outcrop scale, the mapped rocks form a plutonic–volcanic association. Alkali-feldspar granite and syenite are prominent intrusive lithologies, with quartz monzonite and pegmatite also recorded. Rhyolite and trachydacite represent the volcanic or subvolcanic component. The field relationships, together with the structural trends suggest emplacement and subsequent fluid movement within a faulted ring-complex architecture. The precise timing and cross-cutting sequence of individual units, however, require a more explicit field-based contact and dyke chronology (Figure 2).

2. Geochemistry

2.1 Analytical basis and data coverage

Eighteen representative rock samples were collected during geological mapping. Thirteen samples were selected for thin-section preparation and fifteen samples for whole-rock geochemical analysis. Major, trace and reported REE concentrations were determined using a

Rigaku NEX DE energy-dispersive X-ray fluorescence spectrometer at the Department of Geology, Gombe State University. Lithium was determined separately in three selected samples (TB L1, TB L3 and TB L5) using AAS at the Engineering Laboratory of Tatari Ali Polytechnic, Bauchi. The dataset is reconnaissance-scale, comprising of fifteen whole-rock analyses and only three AAS lithium determinations. The source table contains several unusual values and a number of non-detects; consequently, element ranges below, are reported as recorded, with anomalous analyses identified rather than silently corrected.

2.2 Major-element geochemistry and rock classification

The principal felsic assemblage contains 66.1–75.1 wt.% SiO_2 and exhibit high K_2O (4.86–12.7 wt.% in the principal samples) relative to Na_2O (1.6–3.34 wt.%). CaO is generally low (0.351–2.93 wt.%), Fe_2O_3 ranges from approximately 0.885 to 5.57 wt.% in the main assemblage, and MgO is reported as not detected in all fifteen analyses. These characteristics are consistent with the geochemical signatures of evolved, alkali-rich A Type (Aga T & Haruna A.I 2020) granites. The study classifies the samples into granite, syenite, quartz monzonite, rhyolite and trachydacite fields using classification plots, consistent with the field and petrographic observations (Figure 2). TAS/classification scheme reflects an outcome consistiing of granite and rhyolite compositions at approximately 71.3–75.1 wt.% SiO_2, syenitic compositions around 66.1–67.7 wt.% SiO_2, and quartz monzonite–trachydacitic compositions around 68.7–69.3 wt.% SiO_2 (Figure 3 & 4). The major-element plots are interpreted as showing increasing alkalis with SiO_2 and declining CaO, Fe_2O_3, TiO_2 and P_2O_5 in parts of the suite. These compositional trends suggest progressive magmatic differentiation involving feldspar fractionation (Figure 6).

Oxide (wt.%)	**Range in principal felsic samples**	**Geological observation**
SiO_2	66.1–75.1	Felsic to highly evolved compositions
Na_2O	1.60–3.34	Generally subordinate to K_2O
K_2O	4.86–12.70	Potassic enrichment in most principal samples
CaO	0.351–2.93	Generally low; excludes anomalous TB L14B
Fe_2O_3	0.885–5.57	Variable iron content
MgO	ND in all reported samples	May reflect low abundance or analytical reporting/detection limitations
Al_2O_3	10.0–17.1	Excludes anomalous TB L14B and TB L11B

Table 1. Selected major-element ranges from the ED-XRF dataset.

2.3 Trace-element geochemistry

The whole-rock dataset exhibits considerable variation in incompatible and high-field-strength elements. Rb ranges from 9.92 to 1750 ppm, Nb from 15.8 to 905 ppm, Zr from 115 to 3960 ppm and Y from 33.3 to 847 ppm. Sr varies from 7.15 to 495 ppm, while Ba ranges from below detection to 740 ppm. The peak reported Nb (905 ppm), Zr (3960 ppm) and Y (847 ppm) values are substantial exploration indicators, but they are individual whole-rock assay results and should not be interpreted as representative grades without repeat analysis and spatially controlled

sampling. The elevated and variable Rb concentrations, together with low Sr and Ba in several samples, are compatible with feldspar fractionation and the concentration of incompatible elements in evolved residual melts. Rb is generally incompatible in early feldspar-dominated crystallization, whereas Sr is readily incorporated into plagioclase and Ba into K-feldspar. Negative Sr and Eu anomaly, on the primitive-mantle-normalized plot, supports evidence of plagioclase fractionation and the Ba depletion as evidence of K-feldspar fractionation. The coexistence of very high and low values among samples may also reflect multiple intrusive pulses, lithological differences or late-stage redistribution (Figure 7).

Element	Reported range (ppm)	Maximum sample / note
Rb	9.92–1750	TB L16: 1750
Nb	15.8–905	TB L3: 905
Zr	115–3960	TB L3: 3960
Y	33.3–847	TB L11B: 847
Sr	7.15–495	TB L11B: 7.15; TB L1: 495
Ba	ND–740	TB L1: 740
Sn	6.61–70.5	Detected in several samples
Pb	4.84–145	Variable reported concentrations

Table 2. Selected trace-element concentration (Figure 8).

2.4 Rare-earth-element classification and behaviour

The dataset suggests measurable concentrations of selected light rare earth elements (LREE), particularly La, Ce and Nd. La ranges from 67.4 to 437 ppm in samples with reported detections, Ce from 106 to 396 ppm, and Nd from 56.2 to 375 ppm. Pr is reported at 153 ppm in one sample, while isolated detections are also reported for Dy (103 ppm), Tb (72.7 ppm), Er (45.4 ppm) and Yb (68.6 ppm). The dataset therefore supports discussion of selected REE enrichment, especially LREE, but it does not provide a complete and consistently quantified lanthanide suite.

The primitive-mantle-normalized spider diagram demonstrates a relatively cogenetic magma source and LREE enrichment relative to HREE and negative Sr–Eu anomalies. These trends are consistent with evolved felsic magmatism and feldspar fractionation (Figure 9).

3. Tectonic setting and petrogenesis

3.1 Tectonic discrimination

The trace-element discrimination diagrams of Pearce et al, including Nb–Y and Rb–(Nb+Y), demonstrates that the Burji granitoid samples plot predominantly within the within-plate granite (WPG) field (Figure 8). This classification is consistent with an anorogenic, extensional setting and with the broader tectonic interpretation of the Nigerian Younger Granite Province. The reported peralkaline character, high alkali contents, elevated SiO_2 enrichment in Nb, Zr, Y and Rb, is consistent with their A-type affinity.

The samples are interpreted as metaluminous to peralkaline, with agpaitic index values of 0.81–1.92 and reported aluminium saturation index values of 0.52–1.02 (Figure 5).

The available major- and trace-element data are consistent with an evolved A-type, within-plate granitoid suite emplaced in an extensional/anorogenic environment (Figure 8).

3.2 Magmatic differentiation and petrogenetic evolution

The Harker variation diagrams demonstrate a combination of linear and scattered trends. Higher SiO_2 values correspond to elevated Na_2O, K_2O, Rb, Zr, Nb and Y in selected samples, whereas CaO, Sr, Ba, Fe_2O_3, TiO_2 and P_2O_5 tend to decline. The negative CaO–Sr relationship is compatible with the removal of plagioclase during differentiation; decreasing Ba is indicative of K-feldspar fractionation. The scattered character of some plots may suggest compositional heterogeneity, more than one magma pulse, magma mixing or late-stage alteration.

The elevated Rb and HFSE concentrations in selected samples are compatible with concentration of incompatible elements during fractional crystallization. This demonstrates that the more evolved residual melt became enriched in volatile components and incompatible metals, generating conditions favorable for pegmatitic and late-magmatic to hydrothermal processes. The field occurrence of pegmatites, quartz veins and structurally localized rhyolitic bodies is compatible with this model (Figure 6 &7).

3.3 XRF and AAS evidence for lithium and rare-metal enrichment

The AAS analyses provides direct lithium measurements where TB L3 contains 15,320 ppm Li (1.532 wt.% Li), TB L1 contains 12,230 ppm Li (1.223 wt.% Li), and TB L5 contains 7,229 ppm Li (0.7229 wt.% Li). Conversion to Li_2O uses the stoichiometric factor 2.153, giving approximately 3.30, 2.63 and 1.56 wt.% Li_2O, respectively. These are high values for the three selected samples and warrant immediate analytical confirmation. They do not, by themselves, establish the identity of the Li-bearing mineral, the representativeness of the sampled material, or the grade and continuity of any mineralized body.

Sample	Li (ppm)	Li (wt.%)	Calculated Li_2O (wt.%)
TB L3	15,320	1.532	3.30
TB L1	12,230	1.223	2.63
TB L5	7,229	0.7229	1.56

Table 3. AAS lithium results reported in the thesis and stoichiometric Li_2O equivalents (Li_2O = Li × 2.153).

The high lithium results are consistent with evolved felsic magmatism and residual-melt enrichment since Li is commonly incompatible during early crystallization of many felsic magmas and may become concentrated in late residual melts and pegmatitic systems. However, the three AAS assays are selective samples rather than a systematic grid or channel-sampling dataset. For TB L3, the XRF table reports Rb 586 ppm, Nb 905 ppm, Zr 3960 ppm, Y 434 ppm and Sr 144 ppm. For TB L1, the table reports Rb 376 ppm, Nb 15.8 ppm, Zr 211 ppm, Y 56.5 ppm and Sr 495 ppm. These contrasting signatures indicate that lithium enrichment cannot be inferred simply from the magnitude of Nb, Zr or Rb in every sample. Mineralogical identification and spatially controlled sampling are necessary to determine whether Li resides in mica, feldspar, clay/alteration products or another Li-bearing phase.

The combined XRF and AAS results indicate rare-metal fertility at reconnaissance scale. The highest reported Nb, Zr and Y concentrations, together with the measured lithium values and selected LREE concentrations, justify follow-up exploration for Li and associated HFSE–REE. The dataset does not establish an economic deposit or permit resource estimation.

Major Elements

Sample I.D	TB L14B	TB L17	TB L4	TB L16	TB L3	TB L9	TB L2	TB L1	TB L 12 13	TB L15	TB L18	TB L17B	TB L11 B
SiO2	60.5	66.1	66.2	67.7	68.7	69.1	69.3	71.3	71.4	73.9	74.7	75.1	95.6
Na2O	ND	2.72	2.59	2.72	2.32	1.6	2.04	2.47	3.01	3.21	0.208	3.34	ND
MgO	ND	ND	ND	ND	ND	ND	ND	ND	ND	ND	ND	ND	ND
Al2O3	1.56	12.4	12.3	11.4	10	12.9	10.1	11.7	11.7	11.5	17.1	11.1	1.16
P2O5	0.913	1.37	1.49	1.36	1.12	1.32	1.38	1.47	1.5	1.58	1.67	1.56	1.53
K2O	0.247	12.7	9.88	10.4	8.93	8.46	10.4	8.4	8.6	8.03	2.89	4.86	0.238
CaO	35.5	1.51	1.17	0.968	2.93	0.467	2.83	2.73	0.351	0.4	0.448	0.92	0.14
TiO2	0.162	0.112	0.278	0.0814	0.203	0.272	0.174	0.114	ND	0.0232	0.0459	0.0644	0.698
MnO	0.0062	0.0302	0.11	0.0591	0.0329	0.0108	0.0564	0.0511	0.114	0.0097	0.0205	0.0263	ND
Fe2O3	0.665	2.68	5.57	4.81	4.79	5.34	3.32	1.47	2.86	0.885	2.71	2.74	0.245

Trace Element

Ar	ND	ND	ND	ND	ND	ND	ND	ND	ND	ND	ND	ND	ND
Sc	2000	ND	ND	ND	ND	ND	ND	ND	ND	ND	ND	ND	ND
Co	ND	ND	ND	ND	ND	50.8	ND	ND	ND	ND	ND	ND	ND
Ga	14.6	126	137	125	91.1	78.8	93.9	44.4	80.8	119	50.7	102	4.16
Ge	ND	ND	ND	ND	ND	ND	ND	ND	ND	1.77	ND	1.83	ND
Se	1.13	ND	ND	ND	ND	ND	ND	ND	ND	ND	ND	ND	ND
Kr	ND	ND	ND	ND	ND	ND	ND	ND	ND	ND	ND	ND	ND
Nb	100	173	378	215	905	338	271	15.8	122	258	ND	158	403
Tc	ND	ND	ND	ND	ND	ND	ND	ND	ND	ND	ND	ND	ND
In	ND	ND	ND	ND	ND	ND	ND	ND	ND	ND	ND	ND	ND
Te	ND	ND	ND	ND	ND	ND	ND	ND	ND	ND	ND	ND	ND
I	ND	ND	ND	ND	ND	ND	ND	ND	ND	ND	ND	ND	ND
Xe	ND	ND	ND	ND	ND	ND	ND	ND	ND	ND	ND	ND	ND
Cs	ND	ND	ND	ND	ND	ND	ND	ND	ND	ND	ND	ND	ND
Hf	ND	ND	ND	ND	105	ND	ND	ND	ND	ND	ND	ND	69.5
Ta	ND	ND	ND	ND	ND	ND	ND	ND	ND	68.9	ND	ND	43.9
Re	ND	ND	ND	ND	ND	ND	ND	ND	ND	ND	ND	ND	ND
Os	ND	ND	ND	ND	ND	ND	ND	ND	ND	ND	ND	ND	ND
Tl	ND	ND	ND	ND	ND	ND	ND	ND	ND	ND	ND	ND	ND
Bi	ND	ND	ND	ND	ND	ND	ND	ND	ND	ND	ND	ND	ND
Po	ND	ND	ND	ND	ND	ND	ND	ND	ND	ND	ND	ND	15
At	ND	ND	ND	ND	ND	ND	ND	ND	ND	ND	ND	ND	ND
Rn	ND	ND	ND	ND	ND	ND	ND	ND	ND	ND	ND	ND	ND
Fr	ND	ND	ND	ND	ND	ND	ND	ND	ND	ND	ND	ND	ND
Ra	ND	ND	ND	ND	ND	ND	ND	ND	ND	ND	ND	ND	ND
Pm	ND	ND	ND	ND	ND	ND	ND	ND	ND	ND	ND	ND	ND
Sm	ND	ND	ND	ND	ND	ND	ND	ND	ND	ND	ND	ND	ND

Eu	ND	ND	ND	ND	ND	ND	ND	ND	ND	ND	ND	ND	ND
Gd	ND	ND	ND	ND	ND	ND	ND	ND	ND	ND	ND	ND	ND
Tb	ND	ND	ND	ND	ND	ND	ND	ND	ND	ND	72.7	ND	ND
Dy	ND	ND	103	ND	ND	ND	ND	ND	ND	ND	ND	ND	ND
Ho	ND	ND	ND	ND	ND	ND	ND	ND	ND	ND	ND	ND	ND
Er	ND	ND	ND	ND	ND	ND	ND	ND	ND	ND	ND	ND	45.4
Tm	ND	ND	ND	ND	ND	ND	ND	ND	ND	ND	ND	ND	ND
Yb	ND	ND	ND	ND	ND	ND	ND	ND	ND	ND	ND	ND	68.6
Lu	ND	ND	ND	ND	ND	ND	ND	ND	ND	ND	ND	ND	ND
Ac	30.7	25.6	48.4	17.4	ND	29.4	37.2	12.5	22.8	51.2	3.72	34.4	ND
Pa	ND	ND	ND	ND	ND	ND	ND	ND	ND	ND	ND	ND	ND
S	554	619	ND	672	600	601	ND	553	ND	803	527	612	ND
Cl	195	543	495	561	717	361	474	502	339	391	347	357	168
V	ND	ND	ND	ND	ND	ND	ND	ND	ND	ND	71.7	ND	ND
Cr	43.3	ND	ND	ND	ND	ND	ND	ND	ND	ND	32.7	ND	ND
Ni	29.4	14.1	7.65	ND	ND	13	15.5	16.9	ND	8.63	33.1	14.9	19.2
Cu	148	48.8	68	94.7	55.7	89.8	121	96.9	ND	43.3	60.7	42.6	54.4
Zn	65.8	75.6	125	127	165	506	109	117	19.8	31.8	38.1	48.4	16.8
As	20.3	8.95	20.3	ND	ND	ND	13.6	ND	ND	28.9	ND	15.9	ND
Br	ND	ND	ND	ND	ND	ND	ND	ND	ND	ND	ND	ND	ND
Rb	31.6	1170	1480	1750	586	720	1100	376	1610	1060	177	691	9.92
Sr	121	20.3	31.8	15.4	144	44.5	26	495	7.65	9.45	267	15	7.15
Y	273	175	252	233	434	373	422	56.5	377	82.9	33.3	200	847
Zr	361	251	684	130	3960	1240	563	211	456	383	115	392	1750
Mo	ND	ND	ND	48.8	ND	ND	ND	ND	ND	212	11.1	ND	ND
Ru	ND	ND	ND	ND	ND	ND	ND	ND	ND	ND	ND	ND	ND
Rh	ND	ND	ND	ND	ND	ND	ND	ND	ND	ND	ND	ND	ND
Pd	ND	ND	ND	ND	ND	ND	ND	ND	ND	ND	ND	ND	ND
Ag	14.5	ND	ND	15.4	15.9	14	ND	ND	12.7	ND	13.6	ND	9.99
Cd	ND	ND	ND	ND	ND	ND	ND	ND	ND	ND	ND	ND	ND
Sn	19.7	ND	50.5	16.7	9.68	20.1	10.4	6.92	33.3	ND	6.61	34.9	70.5
Sb	ND	ND	ND	ND	ND	ND	ND	ND	ND	ND	ND	ND	ND
Ba	62.9	45.4	112	45.2	476	346	84.5	740	160	ND	262	49.4	57.8
La	99.4	ND	132	ND	163	ND	156	ND	437	67.4	ND	ND	131
Ce	166	ND	287	129	312	190	272	ND	396	110	ND	106	249
Pr	ND	ND	ND	ND	ND	ND	ND	ND	153	ND	ND	ND	ND
Nd	75.1	ND	ND	56.2	175	ND	131	ND	375	ND	ND	ND	93.2
W	ND	ND	ND	ND	ND	ND	ND	ND	ND	ND	ND	ND	ND
Ir	ND	ND	ND	ND	ND	ND	ND	ND	ND	ND	ND	ND	ND
Pt	ND	ND	ND	ND	ND	ND	ND	ND	ND	ND	ND	ND	ND
Au	ND	ND	ND	ND	ND	ND	ND	ND	ND	ND	ND	ND	ND
Hg	ND	ND	ND	ND	ND	ND	ND	ND	ND	ND	ND	ND	ND
Pb	ND	42.5	10.1	78.4	52.4	145	22.4	121	33.9	4.84	30.5	13.8	19
Th	ND	ND	ND	ND	ND	ND	ND	ND	ND	ND	ND	ND	ND
U	ND	ND	ND	ND	ND	ND	ND	ND	ND	ND	ND	ND	ND

Tables 4 Showing Major and Trace Element Geochemical data

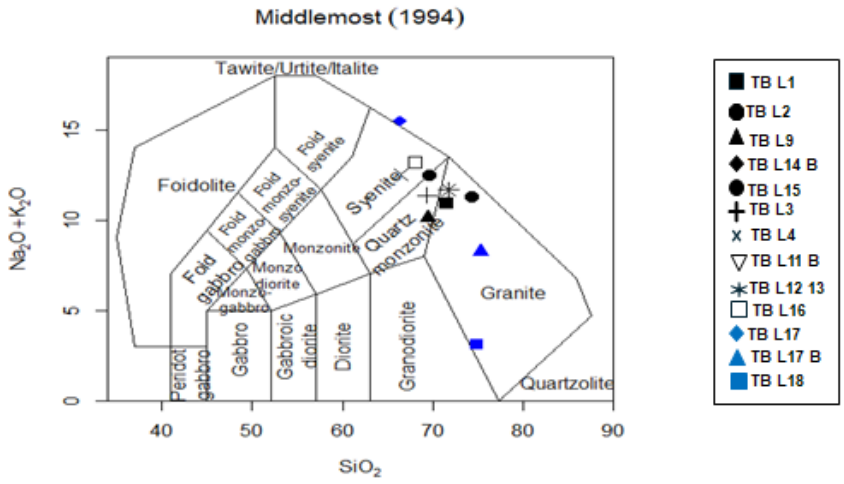


Figure 3. TAS Geochemical classification diagram (Middlemost classification plot) for Plutonic Rocks

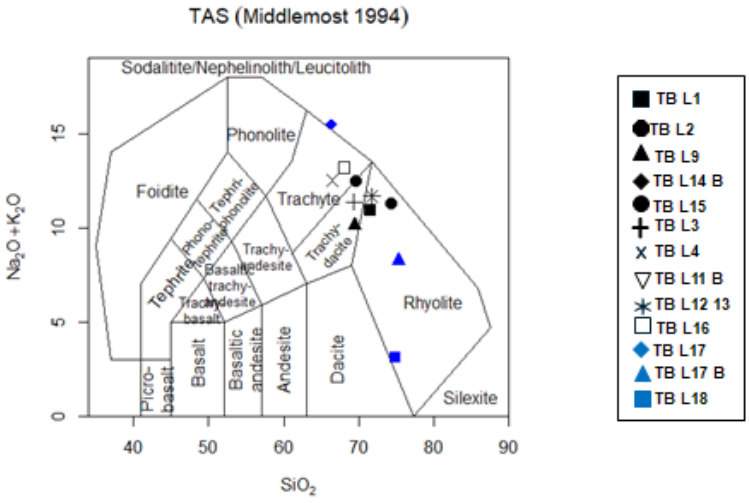


Figure 4. TAS Geochemical classification diagram (Middlemost classification plot) for Volcanic Rocks

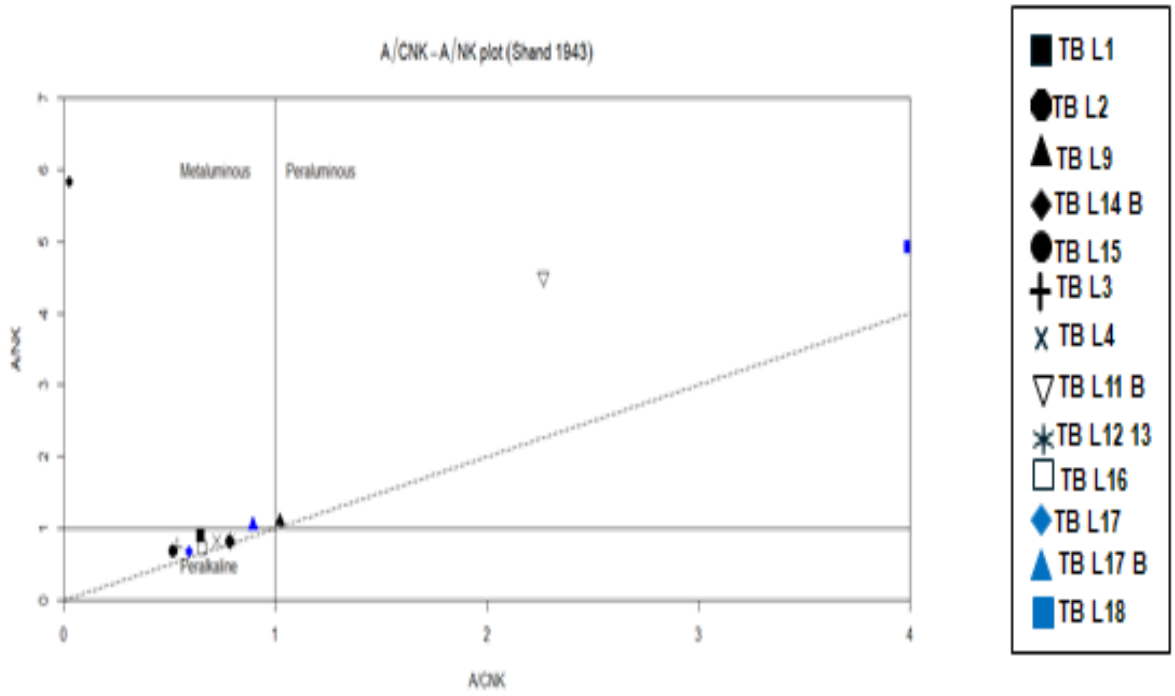


Fig 5 A CNK A NK Plot Shand 1940

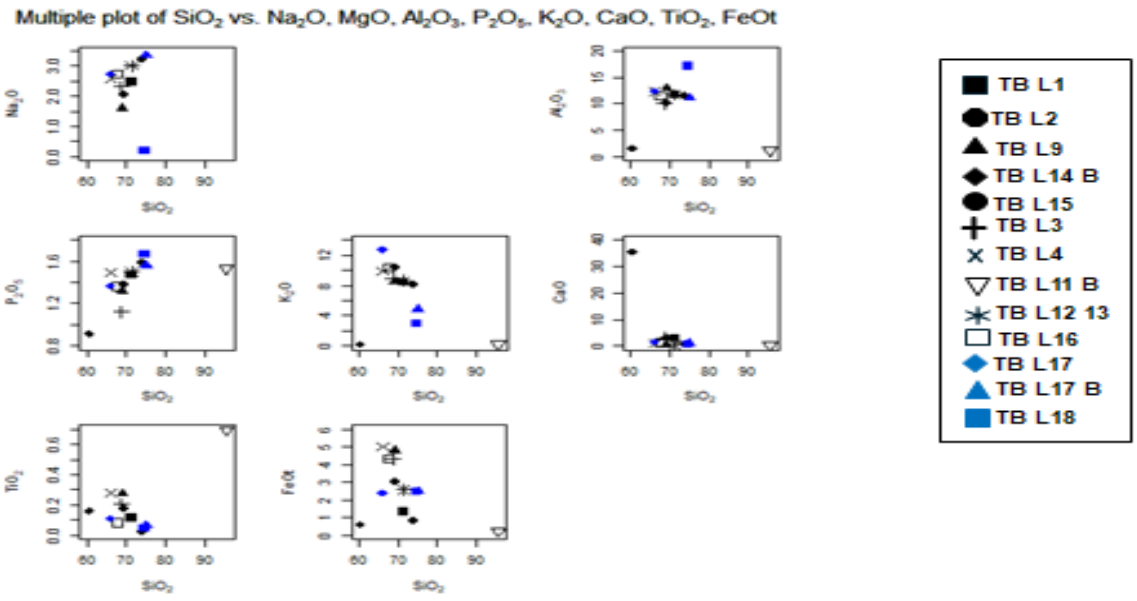


Figure 6 HarkerVariation Diagram for Major Elements

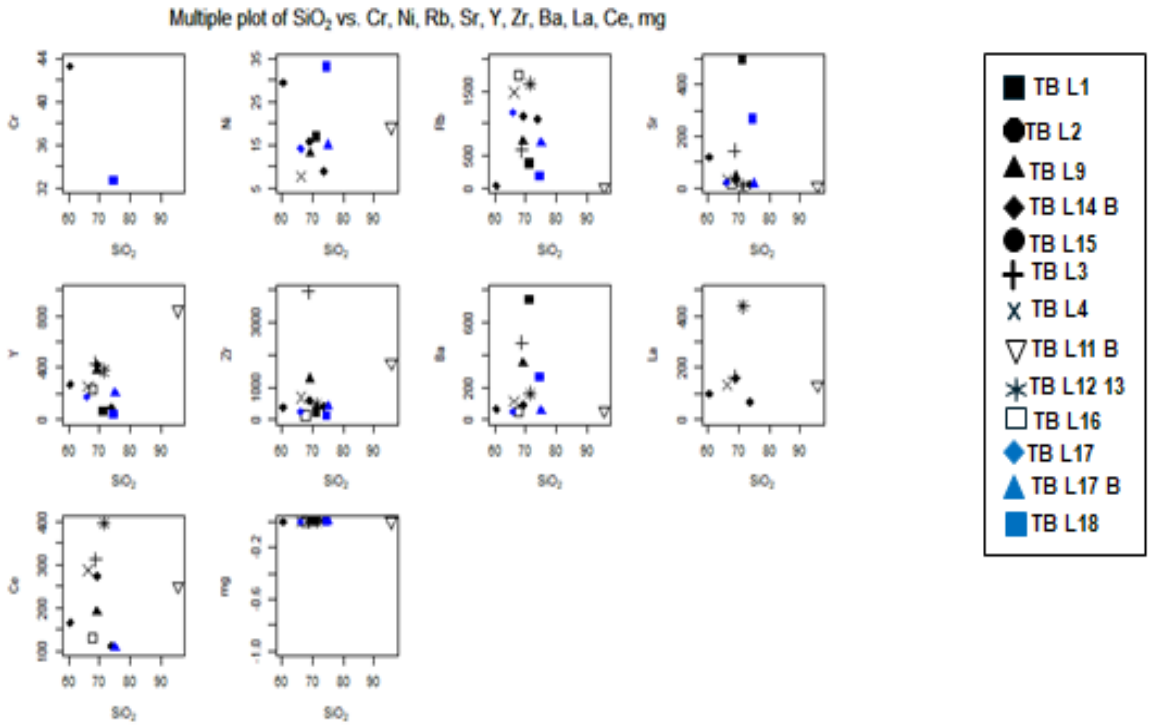


Figure 7 Harker Variation Diagram for Trace Elements

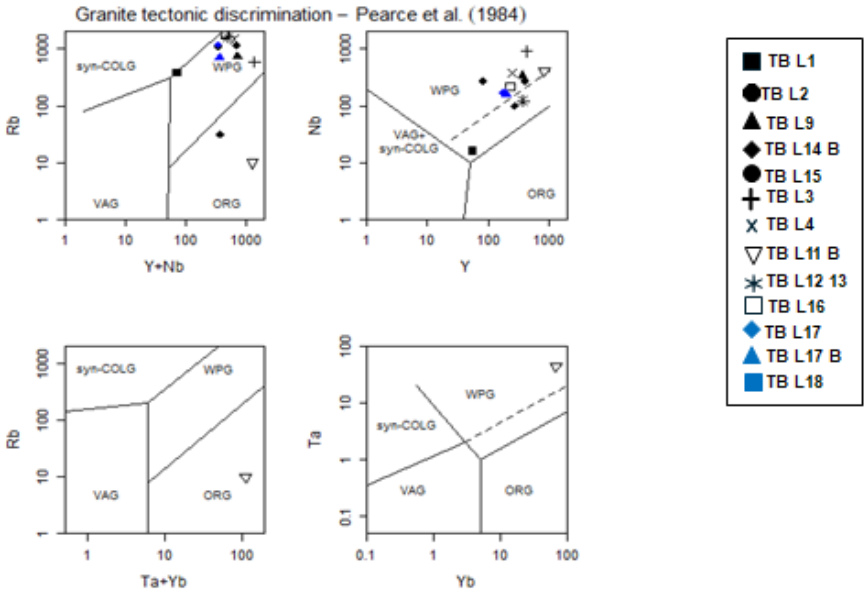


Fig 8 Granite Tectonic Discrimination Plot Pearce et al 1994

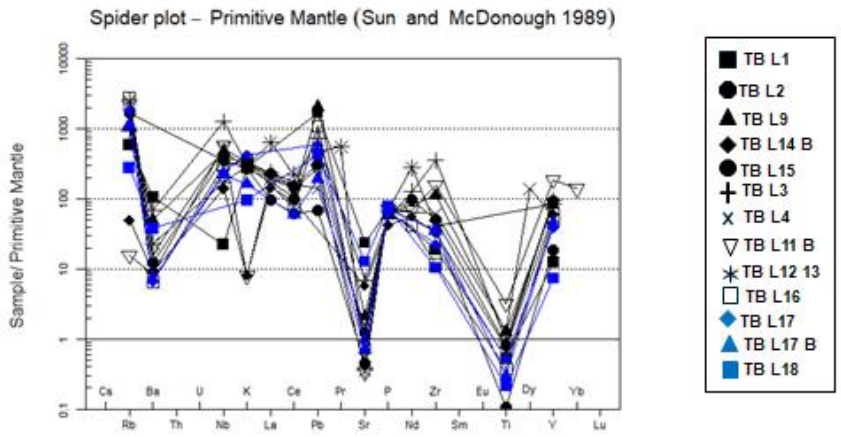


Figure 9 Primitive-mantle-normalized multi-element plot

4.5 Geochemical plots and their petrogenetic significance

The major-element classification and variation plots, alumina-saturation/alkali plots, trace-element variation diagrams, primitive-mantle-normalized spider plots and Pearce-type tectonic discrimination diagrams support an evolved, alkali-rich within-plate granitoid interpretation. Their main implications are summarized below:

Major-element classification plots distinguish granite/rhyolite, syenite and quartz-monzonitic to trachydacitic compositions, broadly matching the field lithologies.

Harker diagrams are interpreted to record progressive differentiation, with feldspar fractionation and removal of Fe–Ti oxides and apatite.

Trace-element variation diagrams show enrichment of Rb and selected HFSE (Nb, Zr and Y) in some samples, consistent with incompatible-element concentration during magmatic evolution.

Primitive-mantle-normalized patterns demonstrate a relatively cogenetic source as well as showing enrichment in incompatible elements, enrichment in LREE to HREE and negative Sr–Eu anomalies.

Pearce-type Nb–Y and Rb–(Nb+Y) diagrams are reported to place the samples in the within-plate granite field.

5. Conclusion

The north-western flank of the Burji Ring Complex comprises an evolved plutonic–volcanic assemblage that includes alkali-feldspar granite, syenite, quartz monzonite, rhyolite, trachydacite and pegmatite. Petrographic textures and field relationships indicate intrusive crystallization, shallow volcanic emplacement and later brittle deformation. The dominant N–S and subsidiary NE–SW and NW–SE structural trends, together with ring-related faults, joints and veins, provide plausible pathways for late-magmatic and hydrothermal fluids.

The principal felsic samples are alkali-rich and generally poor in MgO and CaO. The whole-rock dataset records elevated Rb, Nb, Zr and Y, with selected LREE concentrations also high. The reported Pearce-type discrimination plots classify the suite predominantly as within-plate granites, while the major- and trace-element characteristics are consistent with an evolved A-type affinity in an anorogenic extensional setting. Fractional crystallization, particularly feldspar fractionation, is the principal process invoked to explain the observed incompatible-element enrichment and the reported negative Sr–Eu anomalies.

AAS analyses record 7,229–15,320 ppm Li in three selected samples, equivalent to approximately 1.56–3.30 wt.% Li_2O. These results, together with the highest reported Nb (905 ppm), Zr (3960 ppm), Y (847 ppm) and selected LREE values, identify the Burji complex as a prospective target for follow-up critical-metal exploration. They do not establish a mineral resource, economic grade or continuity. The incomplete REE dataset, limited number of lithium assays, anomalous major-element analyses and unreliable CIPW normative outputs constrain the confidence of the current interpretation. Further work should prioritize repeat assays and QA/QC, systematic channel and grid sampling, complete ICP-MS analysis of the REE–HFSE suite, XRD and SEM–EDS/electron-microprobe identification of Li-, Nb-, Ta-, Zr- and REE-bearing minerals, recalculation of CIPW norms, and fluid-inclusion/isotopic studies of the proposed magmatic–hydrothermal transition. A georeferenced geological map showing lithological contacts, structures and sample locations is also required for a complete journal-ready manuscript.

References

Aga, T., & Haruna, A. I. (2019). The geochemistry and petrogenesis of the Kofayi Younger Granite Complex, Central Nigeria. SSRG International Journal of Geoinformatics and Geological Science, 6(3), 1–6. https://doi.org/10.14445/23939206/IJGGS-V6I3P101

Amuda, A. K., et al. (2021). Petrogenesis of the peralkaline Dutsen Wai and Ropp complexes in the Nigerian Younger Granites: Implications for critical metal enrichments. International Geology Review, 63(16), 2057–2081. https://doi.org/10.1080/00205814.2020.1821250

Bowen, N. L. (1928). The evolution of the igneous rocks. Princeton University Press.

Eby, G. N. (1992). Chemical subdivision of the A-type granitoids: Petrogenetic and tectonic implications. Geology, 20(7), 641–644. https://doi.org/10.1130/0091-7613(1992)020<0641:CSOTAT>2.3.CO;2

Feteha, B. F. E., et al. (2022). Petrogenesis of Neoproterozoic Mo-bearing A-type granites in the Gattar area, northern Eastern Desert, Egypt: Implications for magmatic evolution and mineralization processes. Ore Geology Reviews, 148, 105007.

Helgeson, H. C. (1969). Thermodynamics of hydrothermal systems at elevated temperatures and pressures. American Journal of Science, 267(7), 729–804.

Lindgren, W. (1933). Mineral deposits (4th ed.). McGraw-Hill.

Loiselle, M. C., & Wones, D. R. (1979). Characteristics of A-type granites. Geological Society of America Abstracts with Programs, 11, 468.

McCuaig, T. C., & Hronsky, J. M. A. (2014). The mineral system concept: The key to exploration targeting. Society of Economic Geologists Special Publication, 18, 153–175.

Pearce, J. A., Harris, N. B. W., & Tindle, A. G. (1984). Trace element discrimination diagrams for the tectonic interpretation of granitic rocks. Journal of Petrology, 25(4), 956–983.

Pirajno, F. (2014). Intracontinental anorogenic alkaline magmatism and carbonatites, associated mineral systems and the mantle plume connection. Gondwana Research, 27(3), 1181–1216.

Ridley, J. (2013). Ore deposit geology. Cambridge University Press.

Sibson, R. H. (1992). Implications of fault-valve behaviour for mineralization. In E. R. McClay (Ed.), Thrust tectonics (pp. 541–553). Chapman & Hall.

Vonopartis, L. C., Kinnaird, J. A., Paul, A. M., Nex, P. A. M., & Robb, L. J. (2021). African A-type granites: A geochemical review on metallogenic potential. Lithos, 396–397, 106229. https://doi.org/10.1016/j.lithos.2021.106229

Whalen, J. A., Currie, K. L., & Chappell, B. W. (1987). A-type granites: Geochemical characteristics, discrimination and petrogenesis. Contributions to Mineralogy and Petrology, 95, 407–419.